Triple sum frequency pump-probe spectroscopy of transition metal dichalcogenides

Darien J. Morrow, Daniel D. Kohler, Yuzhou Zhao, Song Jin, and John C. Wright*
Department of Chemistry, University of Wisconsin–Madison, 1101 University Avenue, Madison, Wisconsin 53706, USA

(Received 13 September 2019; revised manuscript received 8 November 2019; published 4 December 2019)

Triple sum frequency (TSF) spectroscopy measures multidimensional spectra by resonantly exciting multiple quantum coherences of vibrational and electronic states. In this work we demonstrate pump-TSF-probe spectroscopy in which a pump excites a sample and some time later three additional electric fields generate a probe field which is measured. We demonstrate pump-TSF-probe spectroscopy on polycrystalline, smooth, thin films and spiral nanostructures of both MoS_2 and WS_2. The pump-TSF-probe spectra are qualitatively similar to the more conventional transient-reflectance spectra. While transient-reflectance sensitivity suffers under low surface coverage, pump-TSF-probe sensitivity is independent of the sample coverage and nanostructure morphologies. Our results demonstrate that pump-TSF-probe is a valuable methodology for studying microscopic material systems.

DOI: 10.1103/PhysRevB.100.235303

I. INTRODUCTION

Pump-probe spectroscopy is a ubiquitous methodology for investigating the dynamics and energetics of excited systems on subpicosecond timescales. In a pump-probe experiment, a pump excites the system of interest and a probe interrogates the evolved system at a later time, T. The differences in the probe signal with and without the pump inform on system evolution. Most analytical merits of a pump-probe experiment, such as sensitivity and selectivity, are determined by the choice of a specific probe methodology, of which there are many [1–10]. The development of coherent multidimensional spectroscopy (CMDS) offers promising possibilities for new probes because CMDS methods can have increased selectivity compared to conventional methods [11–17]. CMDS uses multiple optical interactions to create a multiple quantum coherence within the material whose optical emission is measured. The ability/requirement to couple multiple quantum states together leads to the selectivity inherent within CMDS. By preceding a CMDS pulse sequence by a pump, the selectivity of CMDS can be leveraged as a probe in a "pump-CMDS-probe" measurement [2,3,6,18,19]. In this paper we introduce triple sum frequency (TSF) spectroscopy as a fully coherent probe for material systems by measuring the pump-induced TSF response of model semiconductor systems: transition metal dichalcogenides (TMDCs).

TSF spectroscopy uses three electric fields, E_1, E_2, and E_3, to create coherences at increasingly higher energies. These coherences cooperatively emit a new electric field with frequency $\omega_{out} = \omega_1 + \omega_2 + \omega_3$ in a direction defined by phase matching. Scanning the multiple driving laser frequencies enables collection of a multidimensional spectrum whose cross peaks identify dipole coupling among probed states. The selectivity of TSF is due to the increase in output intensity achieved when the driving fields are resonant with one or more states; multiple-resonance conditions can act as a spectral fingerprint of an analyte [20]. TSF has been used to investigate vibrational and electronic coupling in molecules [21–26], and recently, TSF has revealed the electronic states of MoS_2 and the mixed vibrational electronic coupling of organic-inorganic perovskites [27,28]. We believe that TSF is a promising probe methodology for several reasons: TSF offers complementary information compared to standard techniques such as reflection and absorption [27]; TSF is usable across many different sample morphologies; multiresonant TSF can examine interactions between multiple electronic and/or vibrational states; and pump-TSF-probe is easily extended to microscopy due to the groundwork already laid for multiphoton microscopy [29–31].

In this paper, we use MoS_2 and WS_2 as model systems to demonstrate some of the capabilities of pump-TSF-probe spectroscopy. MoS_2 and WS_2 are well-studied, layered semiconductors in the TMDC family [32]. The band-edge optical spectrum of MoS_2 has two excitonic features labeled A ($\hbar\omega_A \approx 1.8$ eV) and B ($\hbar\omega_B \approx 1.95$ eV) while WS_2 is dominated near the band edge by a single excitonic feature labeled A ($\hbar\omega_A \approx 2$ eV). These features originate from high binding energy excitonic transitions between spin-orbit split bands (cf. absorption spectrum of MoS_2 and inset diagram in Fig. 1) [33–38]. The present work expands upon our previous work on the unpumped TSF response of MoS_2 [27], the extensive body of harmonic generation work on TMDCs (cf. the review by Autere *et al.* [39] and references therein), and the innovative pump–second harmonic generation–probe work accomplished on semiconductors [40–47].

In our previous work on the unpumped TSF response of MoS_2 we noted important differences between the nonlinear TSF probe and conventional linear probes, such as absorption or reflection [27]. One important difference is the scaling with transition dipole, μ, and state density, J: TSF intensity scales as $\mu^8 J^2$, while absorption and reflection scale as $\mu^2 J$. The steep scaling of TSF with transition dipole compared to state density depresses continuum signals and enhances

*wright@chem.wisc.edu

 ©2019 American Physical Society

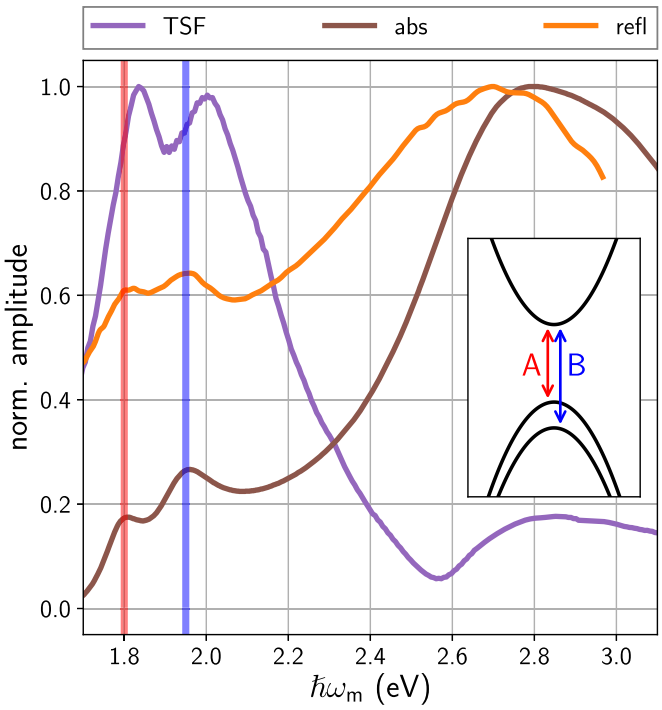

FIG. 1. Normalized amplitude 1D spectra of MoS_2 thin films. The absorption measurement was originally shown in Czech *et al.* [48]. The TSF and reflection contrast measurements were originally shown in Morrow *et al.* [27]. Vertical bars are guides to the eye set at 1.80 and 1.95 eV. The inset is a cartoon of the band dispersion of MoS_2 about the K point. Only the valence bands are shown as spin-orbit-split because the splitting of the conduction bands is generally too small to be observed for MoS_2.

large dipole transitions. The dipole scaling of other CMDS techniques has enabled the measurement of protein structure against large backgrounds when conventional absorption measurements fail [49,50]. The ability of TSF to isolate large dipole transitions is highlighted in Fig. 1 for the example of MoS_2. The absorption and reflection spectra of the MoS_2 thin film are dominated by higher-energy transitions with large joint density of states and low transition moments. Conversely, the TSF spectrum (in this case $\omega_1 = \omega_2 = \omega_3 = \omega_{out}/3$, a third harmonic generation, THG, spectrum) is dominated by the large transition dipole A and B excitonic transitions.

Another important difference between TSF and linear probes is the nature of backward-propagating light. For linear probes, the amount of backward-propagating light (reflection) depends not only on resonance but also on refractive index mismatch, which can result in large background contributions, especially for samples with incomplete surface coverage or rough morphologies. This limitation is important for optically thick samples, where reflection is the only viable linear probe. On the other hand, TSF is well suited for a reflection geometry, where nonlinear pulse propagation effects due to phase mismatch, group velocity mismatch, and absorption are negligible [51]. Furthermore, nonlinear emission in the backward direction is qualitatively different than the direct reflection of incident light, and the refractive index mismatch does not control the measured intensities [52]. For example, we have found that the ratio of reflected TSF emission from MoS_2 films to pure substrate TSF emission is beyond the dynamic range of our experiment as determined by our analog-to-digital-converter (>65 000 : 1) [27]. As a result, a TSF probe provides high contrast signal, resulting in a better signal-to-noise ratio, lower detection limits, and sensitivity to a variety of sample morphologies. This paper highlights these advantages by examining different sample morphologies and surface coverage levels.

The structure of this paper is as follows. In the Theory section we describe the pump-TSF-probe response and compare it to the familiar pump-reflection-probe method. In the Experimental section we describe our spectrometer and our various TMDC samples. In the Results section we present our pump-TSF-probe measurements on TMDCs. We first examine how the multidimensional TSF spectrum is affected by an optical pump. We find that the multidimensional TSF spectrum can be fully described by the one-dimensional pump-THG-probe spectrum. We compare pump-THG-probe to pump-reflectance-probe spectroscopy and we demonstrate that the same pump-induced physics explains both spectra. We then compare the pump-TSF-probe of several TMDC samples that differ in morphology and composition, both demonstrating the versatility of pump-TSF-probe and revealing the strong dependence of morphology on several layer TMDC dynamics. Finally, we discuss how transient-TSF might be used in the future on other systems.

II. THEORY

A. The linear and nonlinear probe

In this section we present the correspondence between the reflectance and TSF of a material. We investigate the phenomenological, microscopic properties that are responsible for the susceptibility and also how the susceptibility dictates the electric field output. Readers interested in first-principles calculations of TMDC nonlinear susceptibility should consult Refs. [53–57]. Our analysis uses standard perturbation theory [58,59]. The material polarization, P, is expanded in orders of the electric field, E:

$$P = \epsilon_0(\chi^{(1)}E + \chi^{(2)}E^2 + \chi^{(3)}E^3 + \cdots), \tag{1}$$

where $\chi^{(n)}$ is the nth-order susceptibility and ϵ_0 is the permittivity of free space. The linear susceptibility, $\chi^{(1)}$, determines the response of linear spectroscopies such as absorption and reflection. The third-order susceptibility, $\chi^{(3)}$, determines the response of nonlinear spectroscopies such as TSF.

Within the dipole approximation, $\chi^{(1)}$ is constructed from a sum over all initial and final states:

$$\chi^{(1)}(\omega_1) = \sum_{a,g} \frac{\mu_{ag}^2}{\Delta_{ag}^1}, \tag{2}$$

where $\Delta_{ag}^1 \equiv \omega_{ag} - \omega_1 - i\Gamma$, μ_{ag} and ω_{ag} are the transition dipole and frequency difference between states a and g, Γ is a damping rate which accounts for the finite width of the optical transitions, and ω_1 is the driving frequency. We see from Eq. (2) that when the driving field is resonant ($\omega_1 = \omega_{ag}$), $\chi^{(1)}$ is large and the interaction with light is strong.

Like Eq. (2), the TSF susceptibility is a sum over states, but we must consider three sequential excitations $g \to a \to b \to c$:

$$\chi^{(3)}(-\omega_{321}, \omega_1, \omega_2, \omega_3) = \mathcal{P} \sum_{c,b,a,g} \frac{\mu_{gc}\mu_{cb}\mu_{ba}\mu_{ag}}{\Delta_{gc}^{123}\Delta_{gb}^{12}\Delta_{ga}^{1}},$$
$$\Delta_{ga}^{1} \equiv \omega_{ag} - \omega_1 - i\Gamma,$$
$$\Delta_{gb}^{12} \equiv \omega_{bg} - \omega_{21} - i\Gamma,$$
$$\Delta_{gc}^{123} \equiv \omega_{cg} - \omega_{321} - i\Gamma, \tag{3}$$
$$\omega_{21} \equiv \omega_2 + \omega_1,$$
$$\omega_{321} \equiv \omega_3 + \omega_2 + \omega_1,$$

where $\mathcal{P}$ is a permutation operator which accounts for all combinations of field-matter interactions. If only the triple sum transition is resonant, we can approximate all other resonance (Δ) terms as constant and arrive at an expression similar to Eq. (2) [27]:

$$\chi^{(3)}(\omega_{123}) \propto \sum_{a,g} \frac{\mu_{ag}^4}{\Delta_{ag}^{123}}. \tag{4}$$

We now consider how the linear and third-order susceptibilities dictate the reflectance and TSF response, respectively. Both relations are formulated using Maxwell's equations via continuity relations (boundary conditions) between the incident, reflected, and transmitted fields. For ease of comparison, we will analyze the simple limit of an extremely thin film (thickness much less than the wavelength of light) on a transparent substrate. We also restrict consideration to normal incidence. Including thickness and angular dependence is straightforward but needlessly complex for our intent of illustrating qualitative differences between methodologies. These conditions are reasonable for many of the samples and experiments we consider here.

With these conditions, the reflectance, R, is related to the thin film linear susceptibility, $\chi^{(1)}$, by [60,61]

$$R \equiv \frac{I_{\text{reflected}}}{I_{\text{incident}}} = \frac{(1 - n_s - A)^2 + B^2}{(1 + n_s + A)^2 + B^2}, \tag{5}$$

in which n_s is the substrate refractive index,

$$A \equiv \frac{\omega_1 \ell}{c}\text{Im}[\chi^{(1)}], \tag{6}$$

$$B \equiv \frac{\omega_1 \ell}{c}\text{Re}[\chi^{(1)}], \tag{7}$$

ℓ is the film thickness (propagation length), and c is the speed of light in vacuum.

Expanding Eq. (5) and keeping only terms linear in $\chi^{(1)}$ shows that the imaginary component of the thin film susceptibility is responsible for contrast from the substrate background:

$$R \approx \frac{(1 - n_s)^2 - 2(1 - n_s)A}{(1 + n_s)^2 + 2(1 + n_s)A}. \tag{8}$$

Equation (8) can be further simplified by Taylor expansion around $A = 0$:

$$R \approx R_0\left(1 - \frac{2}{1 + n_s^2}A\right), \tag{9}$$

where $R_0 \equiv \frac{(1-n_s)^2}{(1+n_s)^2}$ is the reflectance of the substrate-air interface.

Equations (5)–(9) show that reflectance is largely determined by the substrate refractive index, which results in large background. As an example, consider properties appropriate for TMDC thin films encountered here: $\ell \sim 10$ nm and $n_s = 1.45$. Under the optimal conditions of resonant excitation (excitation wavelength ~600 nm and $\chi^{(1)} = i$), $A \approx 0.1$, the thin film gives a maximum contrast from the substrate of $(R - R_0)/R_0 \sim 0.4$. This level of background is typical for reflection studies of TMDC samples [62]. Note that the contrast becomes considerably worse in the case of incomplete sample coverage, where the observed reflection amplitude would be a weighted average of the reflection coefficients. Rough samples introduce scattering which also distort resonance effects of specular reflection.

TSF emission, or nonlinear frequency conversion in general, is qualitatively different from reflectance (or transmittance) because the TSF wave originates from inside the thin film. This difference brings two important consequences to the measured beam: (1) TSF emission is dark in regions where the thin film is not present, and (2) the continuity relations are acutely sensitive to the thin film nonlinear polarization, rather than an incident field [52]. For the aforementioned thin film conditions, the TSF output intensity satisfies the proportionality

$$\frac{I_{\text{TSF}}}{I_1 I_2 I_3} \propto |\chi^{(3)}|^2(\omega\ell)^2, \tag{10}$$

where I_i is the intensity of the ith excitation field [52]. Unlike reflectance, thin film TSF emission obeys the same $\chi^{(3)}$ scaling as the thick film emission case [22], where the film thickness is larger than or close to the wavelength of light, but phase mismatch effects are still small.

B. Pump-TSF-probe and transient-reflectance spectroscopy

We now consider how the different natures of the reflectance and TSF probes result in different, yet similar, pump-probe measurements. For both linear and nonlinear probes, we can describe the pump-induced susceptibility as a perturbation to the unpumped susceptibility:

$$\chi_{\text{pumped}}^{(n)} = \chi_{\text{unpumped}}^{(n)} + \text{d}\chi^{(n)}, \tag{11}$$

where $\text{d}\chi^{(n)} = \chi^{(n+2)}I_{\text{pump}}$ is the small pump-induced perturbation. Pump-probe methodologies often look at relative changes in the probe,

$$\text{signal metric} = \frac{X_{\text{pumped}} - X_{\text{unpumped}}}{X_{\text{unpumped}}}, \tag{12}$$

in which X is the probed quantity. This normalization removes the probe intensity dependence from the signal.

Using reflectance as our probe [Eq. (9)] gives a transient response of

$$\frac{\Delta R}{R} \approx -\frac{R_0}{R}\frac{4\omega\ell}{(1 + n_s^2)c}\text{Im}[d\chi^{(1)}]. \tag{13}$$

This expression shows that our signal metric scales as $\text{Im}[d\chi^{(1)}]$ which is the same as transient transmittance in a

bulk sample (see Appendix A 2 for a derivation). In other words, in the extremely thin film limit, transient reflectance (TR) will have line shapes which are intuitive to those who are used to interpreting bulk transient-transmittance (absorption) measurements. The intuitive correspondence between transient-reflectance and transient-transmittance spectroscopies will break down as $\frac{\omega_1 \ell}{c}|\chi^{(1)}|$ increases—thick samples require a full Fresnel analysis to understand the transient-reflectance line shapes.

With TSF intensity as our probe, we use Eq. (11) and Eq. (10) to arrive at

$$\frac{\Delta I_{\mathrm{TSF}}}{I_{\mathrm{TSF}}} = \frac{|d\chi^{(3)}|^2 + 2|d\chi^{(3)}||\chi^{(3)}|\cos(d\theta)}{|\chi^{(3)}|^2}, \tag{14}$$

where we have used phasor representations of the susceptibilities: $\chi^{(3)} \equiv |\chi^{(3)}|e^{i\theta}$ and $d\chi^{(3)} \equiv |d\chi^{(3)}|e^{i(\theta+d\theta)}$, in which θ can be dependent on probe frequency. If $|d\chi^{(3)}| \ll |\chi^{(3)}\cos(d\theta)|$ we can write

$$\frac{\Delta I_{\mathrm{TSF}}}{I_{\mathrm{TSF}}} \approx 2\frac{|d\chi^{(3)}|}{|\chi^{(3)}|}\cos(d\theta). \tag{15}$$

If the pump changes only the amplitude of $\chi^{(3)}$ ($d\theta = 0, \pi$), the relative change in TSF intensity tracks the relative change in susceptibility. However, if the pump also changes the phase, the amplitude changes can be suppressed. Note that in the case of a $\pi/2$ phase shift, our assumption behind Eq. (15) is invalid. It is important, then, to understand when $\cos(d\theta)$ can be small. In general, θ changes rapidly near resonances; if pump-induced changes shift or broaden a resonance to an extent similar to its linewidth, $d\theta$ will strongly influence the pump-TSF-probe spectrum. In the absence of dramatic resonance changes, line shapes will closely approximate $d\chi^{(3)}/\chi^{(3)}$.

To anticipate the spectra of each technique, it is useful to consider the case of a single Lorentzian resonance perturbed by the pump. For a small perturbation to line-shape parameter $\lambda \in \{\Gamma, \omega_{ag}, \mu\}$, we can construct $d\chi^{(n)}$ using the derivative

$$d\chi^{(n)} = \frac{\partial \chi^{(n)}}{\partial \lambda} d\lambda. \tag{16}$$

In the appendices we derive analytical expressions for the line shapes expected from transient-TSF, transient-reflectance, and transient-transmittance spectroscopies in this single-resonance limit. Numerically calculated spectra are shown in Fig. 2 for three different types of perturbations:

(1) An increase in the transition dipole, $d\mu > 0$. State filling and Coulomb screening lead to a decrease in exciton transition dipoles (opposite of change shown in the figure). Note that changes in state density will cause the same line shape as transition dipole changes.

(2) An increase in the resonance frequency, $d\omega_{ag} > 0$. Band-gap renormalization or Coulomb screening can decrease or increase an exciton resonance frequency.

(3) An increase in the dephasing rate, $d\Gamma > 0$. Pump-excited carriers can scatter with probe excitations, causing the dephasing rate of a transition to increase.

The transient-reflectance spectra [see Fig. 2(a)] are easily interpreted because changes in $\mathrm{Im}[\chi^{(1)}]$ correlate with changes in absorptive cross section [Eq. (9)]. Interpretation of $\Delta R/R$ line shapes mirrors the traditional interpretation of differential transmission, $\Delta T/T$, for bulk samples obeying Beer's law. Increasing the dipole strength (red line) increases reflectance (positive $\Delta R/R$), with a line shape mirroring the unpumped transition. Resonance redshifts (green line) increase reflectance to the red and decreases reflectance to the blue. Line-shape broadening (blue line) decreases reflectance in the center of the resonance but increases reflectance on the wings.

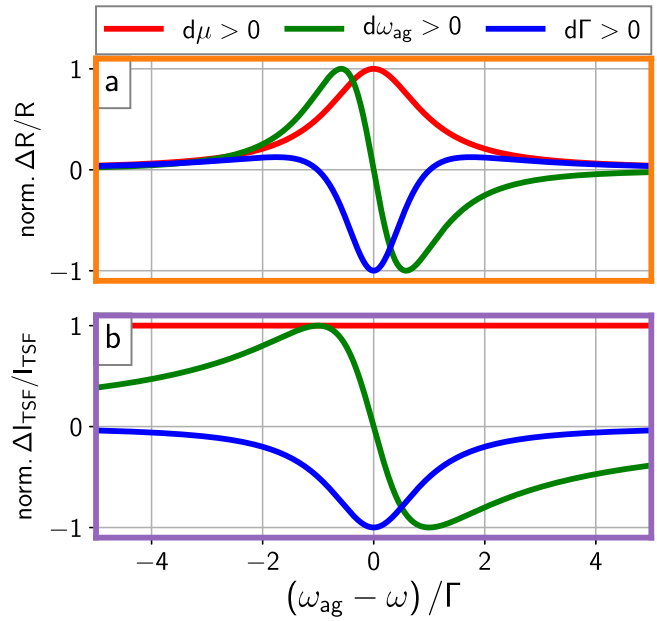

FIG. 2. Calculated transient line shapes for a single, complex Lorentzian resonance (see Appendices A 1 and A 2). (a) The transient-reflectance spectrum. (b) The transient-TSF spectrum. The spectra are produced by perturbing μ, ω_{ag}, or Γ by a factor of 10^{-5}.

The transient-TSF line shapes [Fig. 2(b)] have similar interpretations. Increases in the transition dipole (red line) increase TSF (positive $\Delta I/I$). Unlike reflectance, the increase results in a constant $\Delta I/I$ offset. This is because the unpumped I_{TSF} line shape has no background from the substrate and so its line shape is sharply peaked and matches that of ΔI. Line-shape broadening (blue line) and blueshifting (green line) again mirror the behavior of $-\Delta T/T$, but the $\Delta I/I$ line shapes are noticeably broader than $\Delta R/R$. Since TSF is sensitive not only to the imaginary component but also the dispersive real component of $\chi^{(3)}$ [Eq. (15)], the resulting line shapes are intrinsically broader. In general, for the same dephasing rate, the transient-TSF line shapes are broader than the transient-transmittance and transient-reflectance line shapes.

III. EXPERIMENTAL

A. Ultrafast measurements

Our experimental setup uses an ultrafast oscillator seeding a regenerative amplifier (Spectra-Physics Tsunami and Spitfire Pro, respectively) to produce ~35 fs pulses centered at 1.55 eV at a 1 kHz repetition rate. The amplifier output separates into three arms. Not all arms are used in every experiment. Two arms are optical parametric amplifiers

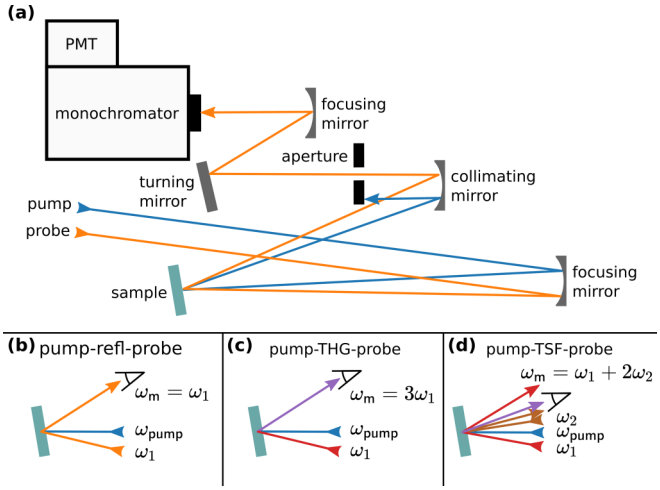

FIG. 3. Overview of the pump-probe experiments in this work. (a) Schematic of the focusing and collection assembly (not to scale). The optical axis is ∼9° from the sample surface normal. PMT: photomultiplier tube. Also shown are the three excitation geometries used in this work: (b) pump-reflection-probe, in which the specular probe (ω_1) reflection is measured; (c) pump-THG-probe, in which the third harmonic signal ($3\omega_1$) travels in the same direction as the fundamental incident probe; and (d) pump-TSF-probe, in which signal is isolated in the $2k_1 + k_2$ direction. The ◁ symbol denotes the collected beam direction (isolated with an aperture). For the sake of clarity, some reflections are not shown.

(Light-Conversion TOPAS-C) which create tunable pulses of light from ∼0.5 to ∼2.1 eV with spectral width on the amplitude level of FWHM ≈ 46 meV; absorptive filters and wire grid polarizers are used to isolate light of the desired color [63]. The third arm frequency doubles the output of the amplifier to create pulses centered at 3.1 eV in a β-barium-borate crystal. Each arm has its own mechanical delay stage and optical chopper. All pulses are then focused onto the sample with a 1 m focal length spherical mirror. The spatially coherent output (either the reflected probe or the triple sum of the probe) is isolated with an aperture in the reflected direction (sometimes referred to as an *epi* experiment), focused into a monochromator (Horiba Micro-HR) and detected with a thermoelectrically cooled photomultiplier tube (RCA C31034A). Figure 3 diagrams the focusing and collection geometry used in this work. A dual-chopping routine is used to isolate the desired differential signal [64]. The color-dependent time of flight for each arm is corrected by offsetting the mechanical delay stages for each combination of pump and probes colors. We use a reflective geometry for our TSF measurements in order to minimize phase-mismatch effects [51,65]. Unless otherwise noted, the pump fluence in these measurements is ∼100 μJ/cm^2. In Appendix D we show that this pump fluence is sufficiently small that higher-order nonlinear pump-induced effects can be neglected. The visible probe beam for the reflectance-probe experiments has a fluence of ∼2 μJ/cm^2 while the NIR probe lasers for the TSF-probe experiments have a fluence of ∼1000 μJ/cm^2. All beams are hundreds of microns wide at the sample. Our acquisition [67] and workup [68] software are built on top of the open-source, publicly available Scientific Python ecosystem [69–71].

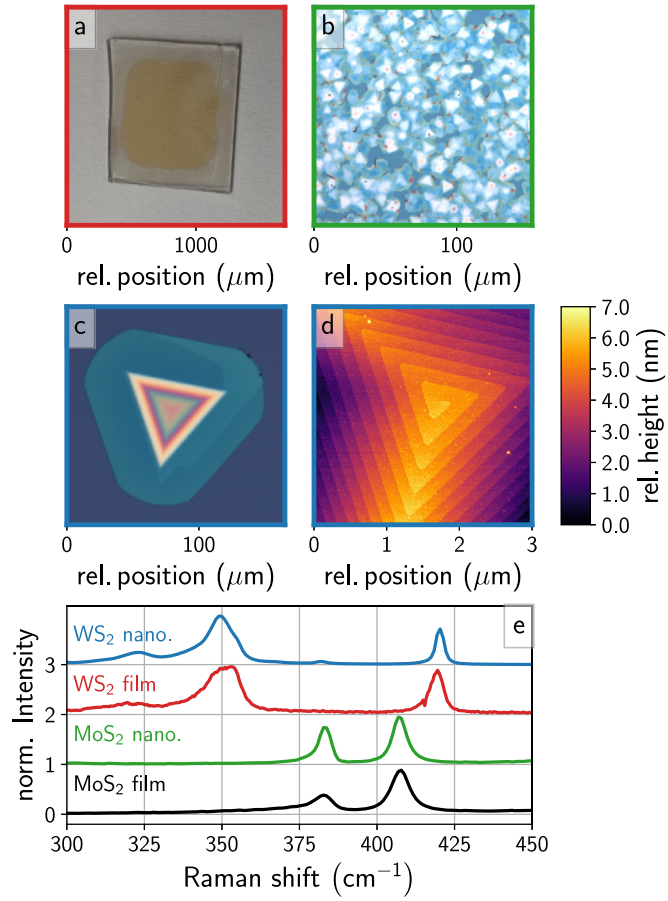

FIG. 4. TMDC sample characterization. (a) Photograph of the WS_2 film explored in this work. (b) Optical microscope image of the MoS_2 nanostructures explored in this work. (c) Optical microscope and (d) atomic force microscope image of the WS_2 nanostructure explored in this work. (e) Raman spectra of each sample; the maximum of each Raman spectrum is normalized to 1 and then offset for ease of comparison.

B. Sample preparation and characterization

Polycrystalline MoS_2 (WS_2) films were prepared by first e-beam evaporating 2 nm of Mo (W) onto a fused silica substrate and subsequent sulfidation in a tube furnace at 750 °C for 10 (30) minutes [48]. Note that this exact MoS_2 thin film sample was previously explored in Morrow *et al.* [27]. Following the methods detailed in Zhao and Jin [72], WS_2 (MoS_2) nanostructure samples on 300 nm SiO_2/Si substrates were prepared using water vapor assisted chemical vapor transport growth by heating 100 mg WS_2 (MoS_2) powder to 1200 °C at 800 torr in a tube furnace in which water vapor was produced by heating 1 g $CaSO_4 \cdot 2H_2O$ powder to 150 °C (120 °C) using heating tape wrapped around the tube furnace; 100 sccm argon was used as the carrier gas during the reaction.

Figure 4 shows optical microscope (Olympus BX51M) images, atomic force microscope (Agilent 5500) data, and Raman spectra (LabRAM Aramis, Confocal Raman/PL Microscope, 2.33 eV excitation) of the samples. The Raman spectra show the common E^1_{2g} and A_{1g} modes seen in WS_2 and MoS_2 at the frequencies expected for many-layer to bulk morphologies [73–75]. The polycrystalline thin films

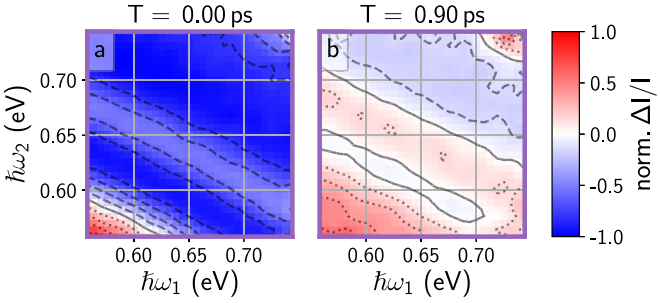

FIG. 5. Pump-TSF-probe spectra of a MoS_2 thin film at 0 ps (a) and 0.90 ps (b) delay between pump and probe interactions. In both frames $\hbar\omega_{\text{pump}} = 3.1$ eV with a fluence of 120 μJ/cm^2, $\omega_m = \omega_1 + 2\omega_2$, and $\vec{k}_{\text{out}} = \vec{k}_1 + 2\vec{k}_2$.

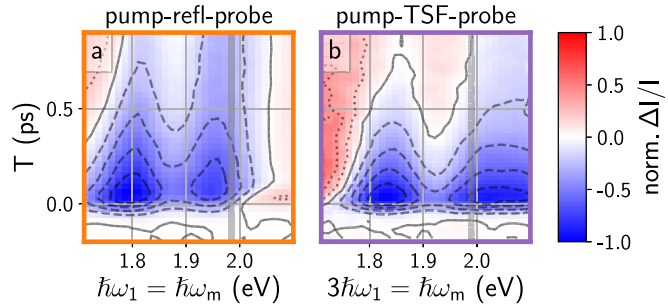

FIG. 6. Comparison of transient-reflectance spectroscopy (a) to transient-TSF spectroscopy (b) for a MoS_2 thin film. In both frames $\hbar\omega_{\text{pump}} = 1.98$ eV, as indicated by the vertical gray line. Each plot has its own color map extent: red (dotted contours) signifies $\Delta I/I > 0$, white (solid contour) signifies $\Delta I/I = 0$, and blue (dashed contours) signifies $\Delta I/I < 0$.

(∼10 nm thick) are continuous, flat, and smooth samples that are much larger than the spot size of our lasers [see Fig. 4(a)]. Each MoS_2 nanostructure [Fig. 4(b)] is a few microns wide and sparsely scattered across the substrate. The nanostructures exhibit a wide range of morphologies from screw-dislocation spirals to stacked plates. The WS_2 nanostructure [Figs. 4(c) and 4(d)] is a single screw-dislocation spiral which is 84 nm (∼120 layers) thick and ∼150 μm wide. TMDC screw-dislocation spirals are known to have excellent optical harmonic generation abilities [76–79]. Note that the perceived colors of the nanostructures in Figs. 4(b) and 4(c) are due to thin film interference effects from the combination of the pyramid nanostructures, which have a large change in height across the structure, and the SiO_2/Si substrates; this class of effects has previously been explored for monolayers and nanostructures [80–82].

IV. RESULTS AND DISCUSSION

A. MoS_2 thin film: Transient-TSF

We first examine the effect of a pump on the multidimensional TSF spectrum, in which ω_1 and ω_2 are independently scanned. The output frequency of the TSF probe, $\omega_m = \omega_1 + 2\omega_2$, covers the range of the *A* and *B* excitons (1.65–2.25 eV). We explore this dependence with a MoS_2 thin film. In this film, the unpumped multidimensional spectra exhibit singly resonant features that depend only on the output triple sum frequency [e.g., Eq. (4)] [27]. There are no cross peaks in the unpumped TSF spectrum because MoS_2 *A* and *B* excitons do not have the correct symmetry for our excitation beams to couple together. Like the unpumped spectrum, we found that the pump-TSF-probe spectrum depends only on the triple sum frequency, regardless of pump-probe delay time. Pump-TSF-probe spectra of the MoS2 thin film at two different delays are shown in Fig. 5 ($\hbar\omega_{\text{pump}} = 3.1$ eV). At both delay times, all features run along lines of constant output color (slope of $-1/2$). We explored the multidimensional probe spectra at other frequency and *T* combinations (output energies up to 3 eV and population times up to 100 ps); all features found are defined solely by the output color.

Given the similarities in band structure, we expect this result to be general to all TMDCs. The simplicity of the TSF and pump-TSF-probe spectra motivate the use of Eq. (4) and its associated pump-THG-probe analysis which was discussed in the Theory section. Since the output color seems to uniquely determine the observed spectra, we restrict ourselves to the case $\omega_1 = \omega_2 = \omega_m/3$ (pump-THG-probe) for the rest of this work. We will understand the line shapes present in Fig. 5 by understanding the line shapes of the pump-THG-probe spectroscopy presented in the next section.

B. MoS_2 thin film: Transient-THG and transient reflectance

Here we consider the pump-reflectance-probe and the pump-TSF-probe side by side to understand the differing selectivities of both methods. We first compare both probe methodologies using a single pump color. Figure 6 shows both the pump-reflectance-probe (left) and the pump-TSF-probe (right) response of the MoS_2 thin film with pump excitation at the *B* exciton. Note that horizontal $3\omega_1$ slices through Fig. 6(b) are almost equivalent to the diagonal, $\omega_1 = \omega_2$ slices of Fig. 5; they differ only in the use of different pump colors.

The TR and pump-THG-probe responses of Fig. 6 are qualitatively similar. Our analysis in the Theory section indicates that phenomena such as shifting and broadening will lead to similar line shapes between the two spectroscopies while state density and dipole decreases will look different between the two spectroscopies—so our observed response is likely due to shifting and broadening of the underlying excitonic resonances. In both spectra, the measured intensity at the *A* and *B* excitons decreases when the pump is on ($\Delta I/I < 0$). The intensity decreases dominate at $T = 0$, then decay over ∼500 fs to form spectra that undulate between positive and negative values. These undulating spectra persist for several picoseconds (data not shown).

The minima of the transient-THG spectra are blueshifted relative to the corresponding minima observed in the transient-reflectance spectrum, but roughly agree with the peak positions of the unpumped THG spectrum (Fig. 1). The *A* and *B* peaks of the unpumped THG spectrum are blueshifted by ∼50 meV compared to the absorption/reflection spectrum. We cannot explain why the maxima of the THG and absorption/reflection spectra are different by ∼50 meV, but we note that Wang *et al.* [83] also observed this same unexplained blueshift in their THG measurements.

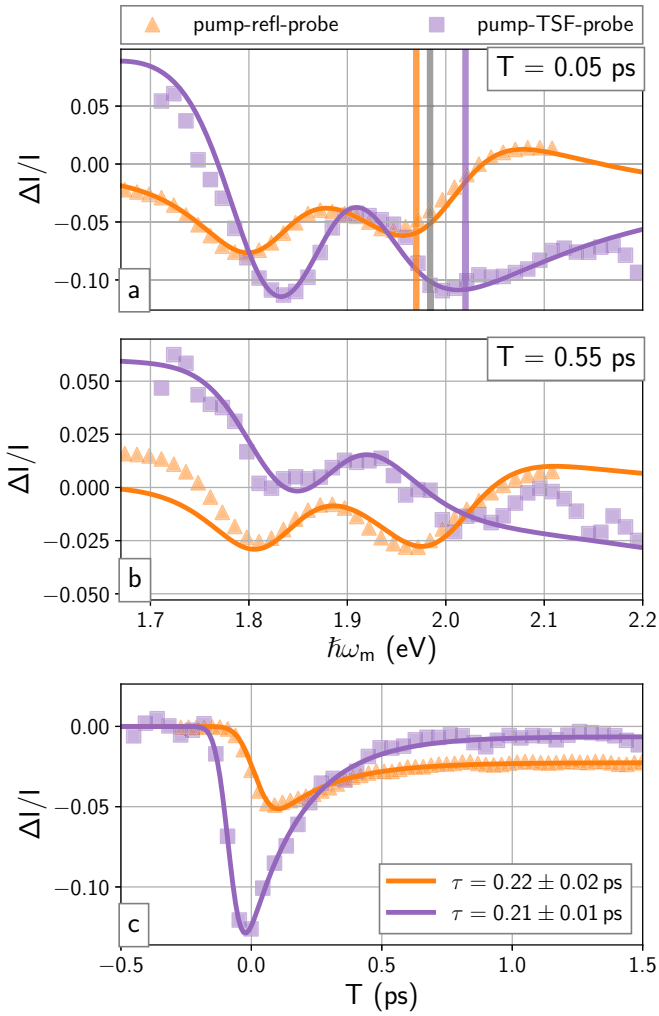

FIG. 7. Comparison of spectral and temporal line shapes with $\hbar\omega_{\text{pump}} = 1.98$ eV (gray vertical line). Spectral line shapes in (a) and (b) are acquired with delay times of 0.05 and 0.55 ps, respectively. Dynamics in (c) are acquired at probe energies indicated by the vertical lines in (a) (1.97 and 2.02 eV for pump-refl-probe and pump-TSF-probe, respectively). Solid lines in each plot are calculated from the models described in the main text and Appendix B.

To understand the spectral and temporal information in Fig. 6, we examine transients at fixed probe frequencies and spectra at fixed time delays in Fig. 7. For both cases, we use simple models to ensure that standard physical arguments can explain our observations. Specifically, we show that the behavior of both probes can be understood with the same underlying system changes.

We first consider the spectral slices. The technical details of the spectral line-shape model [results shown as solid lines in Figs. 7(a) and 7(b)] are discussed in Appendix B. In both spectroscopies, the line shape at $T \approx 0$ [Fig. 7(a)] can be explained by a ∼10 meV redshift, slight broadening, and slight amplitude decreases of the A and B resonances. In order to describe the pump-TSF-probe line shape in Fig. 7(b) we incorporated an additional excited-state absorption (ESA) background. We attribute the additional ESA to excitation of near-band-edge carriers (conduction band electrons, valence band holes, or excitons) upon pump photoexcitation and subsequent relaxation. We attribute the redshift to carrier-induced band-gap renormalization (BGR), which was previously predicted and observed by many in monolayer TMDCs [8,84–87]. The line-shape broadening upon excitation is common in semiconductors and has been previously observed by Refs. [88,89] in TMDCs. The amplitude decrease is likely due to state/band filling from the photocarriers.

TABLE I. Results from fitting Eq. (17) to the dynamics shown in Fig. 7(b). FWHM = full width at half maximum of the instrument response function.

	pump-refl-probe	pump-TSF-probe
$\hbar\omega_m$ (eV)	1.97	2.02
τ (ps)	0.22 ± 0.02	0.21 ± 0.01
FWHM (ps)	0.125 ± 0.009	0.095 ± 0.006

A short time after excitation, $T = 0.55$ ps, the probe spectra change [Fig. 7(b)]: the line shapes are reproduced by a few meV redshift, no broadening, and no amplitude decrease. The simultaneous decrease in broadening, BGR, and state/band filling suggests that the majority of photocarriers have relaxed within several hundred femtoseconds, a curious dynamic that will be explored throughout this paper. Importantly, the interpretation of both probe methodologies is consistent.

Dynamics were described by an exponential decay and a static offset:

$$\frac{\Delta I}{I}(T) = \left[A_0 \exp\left(-\frac{T}{\tau}\right) + A_1\right]\Theta(T - t_0), \qquad (17)$$

in which Θ is the Heaviside step function. We convolve Eq. (17) with an instrument response function, which we approximate as Gaussian. Results are shown as solid lines in Fig. 7(c). Like the spectral line shapes, the dynamics of both probe methods are consistent (Table I). The fast dynamic that changes the probe spectra in Figs. 7(a) and 7(b) has a time constant of ∼200 fs [90]. Dynamics on this timescale have previously been attributed to several mechanisms, including carrier trapping [91–93], carrier-carrier scattering [88,94], carrier-phonon scattering [95–97], free-carrier screening effects [89,98], and exciton formation [98]. The longer dynamic in Fig. 7(c), which we treat as an offset, A_1, is common in single-crystal ultrathin TMDC samples [92,98].

Figure 8 shows the response from both TR and transient-THG spectroscopies for different combinations of pump and probe frequencies when $T = 50$ fs. Figure 8(a) is a very similar measurement to Refs. [48,99–105] where "traditional" coherent multidimensional spectroscopies were accomplished on TMDCs using a single electric field interaction as a probe; this measurement similarity is not the case for Fig. 8(b) in which TSF acts as the probe with three electric field interactions. Nevertheless, both of our spectroscopies in Fig. 8 have a similar dependence on the pump frequency—this can be seen by comparing vertical slices of Figs. 8(a) and 8(b) (these horizontal slices are analogous to horizontal slices of Fig. 6) [106]. The line shapes of our two spectroscopies change smoothly as a function of $\hbar\omega_{\text{pump}}$—there are no distinct

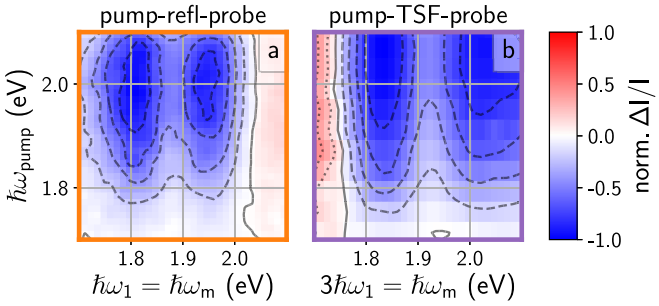

FIG. 8. Comparison between transient-reflectance spectroscopy (a) and transient-TSF spectroscopy (b) of a MoS_2 thin film. In both frames $T = 50$ fs.

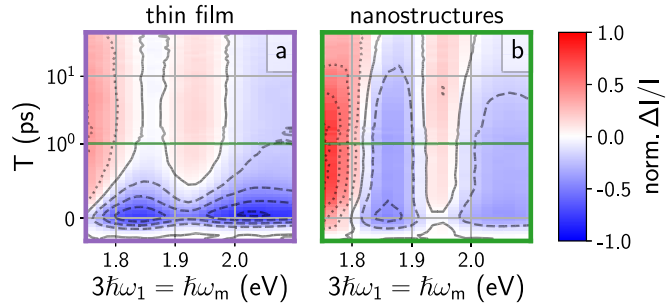

FIG. 9. Pump-TSF-probe spectra of a MoS_2 thin film (a) and a MoS_2 spiral nanostructure ensemble (b). The temporal axis has linear scaling until 1 ps (horizontal green line) and then logarithmic scaling until the end (50 ps). In both frames $\hbar\omega_{pump} = 3.1$ eV with a fluence of 120 μJ/cm^2.

contributions from the A or B resonances along the pump axis. The lack of structure along the pump axis mirrors the results of transient grating measurements on a MoS_2 thin film [48]. The general insensitivity to pump color suggests that BGR is a large contributor to the pump-induced changes. BGR is determined by Coulomb interactions, which are less sensitive to the explicit electron and hole occupation than, for instance, Pauli blocking effects.

Conversely, small but noticeable dependencies on ω_{pump} suggest secondary contributions to the TR and transient-TSF spectra. For instance, when $\hbar\omega_{pump} \approx 1.8$ eV $\approx \hbar\omega_A$, the decreases in intensity at $\omega_{out} = \omega_A$ are ~15% larger than at $\omega_{out} = \omega_B$ for both TR and pump-TSF-probe. When $\hbar\omega_{pump} \approx \hbar\omega_B$, however, both A and B have similar decreases in intensity. We believe that band/state filling (bleaching) can account for the observed asymmetries in the decreases in intensity. The MoS_2 valence band is energetically split for different hole spins, but the conduction band is energetically degenerate for electron spins (cf. the inset in Fig. 1). The A transition and B transition share neither valence nor conduction bands, so state/band filling is not shared between transitions. When the pump is resonant with the A transition, the bleach of the B transition is not direct and is expected to be smaller, in agreement with our measurements. Some bleaching is allowed through intervalley scattering, but valley depolarization measurements suggest that these timescales are much longer than our pump-probe delay time (50 fs) and thus not significant [107–109]. When the pump is resonant with the B transition, it will also directly excite hot excitons or free electrons/holes from the A band, which explains why the effects on the A and B transitions are similar for these pump colors. These observations are all consistent with the line-shape analysis of Fig. 7(a), in which redshifts (BGR) played a significant, but not complete, role in the line shape.

Guo *et al.* [105] also found asymmetries in the cross peaks of their multidimensional spectra of monolayer MoS_2 at 40 K. They attribute the asymmetric cross peaks and their dynamics to an exchange interaction between A and B excitons. This effect does not explain our results because the exchange interaction requires simultaneous populations of A and B excitons, which is not the case for $\omega_{pump} \approx \omega_A$.

C. MoS_2 and WS_2 nanostructures

In this section we investigate the effects of sample morphology on pump-TSF-probe spectroscopy by comparing all the samples shown in Fig. 4. We first compare spectra of the previously discussed thin film with an ensemble of spiral nanostructures grown via a screw-dislocation driven growth method [Fig. 4(b)]. The goal of this comparison is to broadly demonstrate that the spectra and dynamics observed with transient-TSF are sensitive to the specifics of sample morphology. We then compare the transient-TSF and TR response of both a WS_2 thin film and a single WS_2 screw-dislocation nanostructure.

1. *Transient-THG of a* MoS_2 *thin film vs nanostructures*

Figure 9 shows the probe frequency versus delay time response of the thin film [Fig. 9(a)] and nanostructure [Fig. 9(b)]. Both spectra show similar spectral line shapes near zero delay with decreases at the A and B features. The nanostructures spectrum [Fig. 9(b)] demonstrates narrower peaks and greater increase in TSF intensity to the red of the A exciton resonance compared to the thin film [Fig. 9(a)]. The nanostructures exhibiting narrower features indicate that the thin film has more structural inhomogeneity. While both samples show similar line shapes at $T = 0$, they exhibit drastically different dynamics.

Figure 10 shows a single temporal trace through the data shown in Fig. 9 for each sample morphology. The thin lines are the measured data and the thick lines are fits using Eq. (17). We recover exponential decay time constants of 0.34 ± 0.02 ps for the thin film and 12.7 ± 0.8 ps for the nanostructures. The morphology strongly affects dynamics. We speculate that the dramatic differences in timescales are related to the density of grain boundaries, which can affect carrier scattering, recombination, and/or trapping [91]. The grain size of the thin film is on the order of 100 nm^2 while that of the nanostructures is on the order of 10–100 μm^2. We believe that carrier trapping or defect-assisted annihilation is the main source of dynamics in Fig. 10; a carrier once it has been trapped/annihilated is not able to efficiently screen the electron-hole Coulomb interaction, so BGR is lessened and the observed differential response is decreased.

There is a low-amplitude, rapid dynamic present for each sample in Fig. 10 that is not captured by our single-exponential fit; we attribute this rapid dynamic to hot carriers (the carriers have ~1 eV excess energy upon photoexcitation)

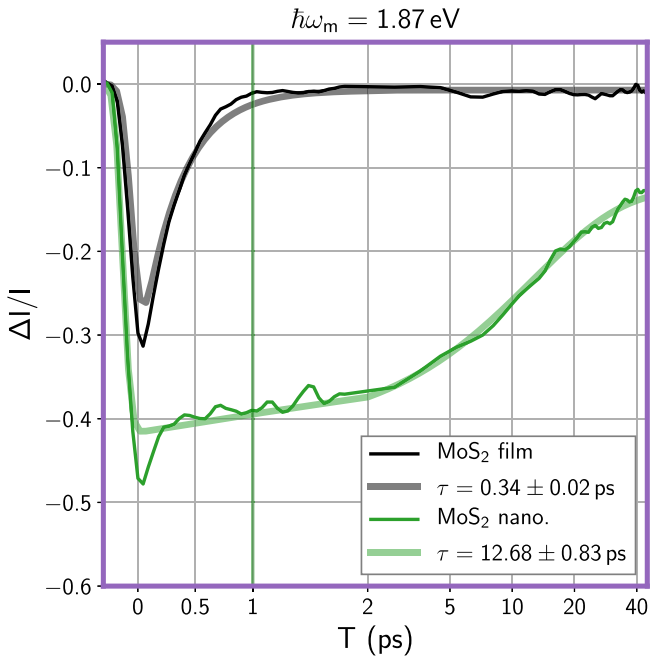

FIG. 10. Pump-TSF-probe of a MoS_2 thin film and an ensemble of spiral nanostructures. The temporal axis has linear scaling until 1 ps (green line) and then logarithmic scaling until the end (50 ps). This figure displays 1D slices out of Fig. 9 in which the pump is set to $\hbar\omega_{\text{pump}} = 3.1$ eV while the probe is set to $3\hbar\omega_1 = \hbar\omega_m = 1.87$ eV.

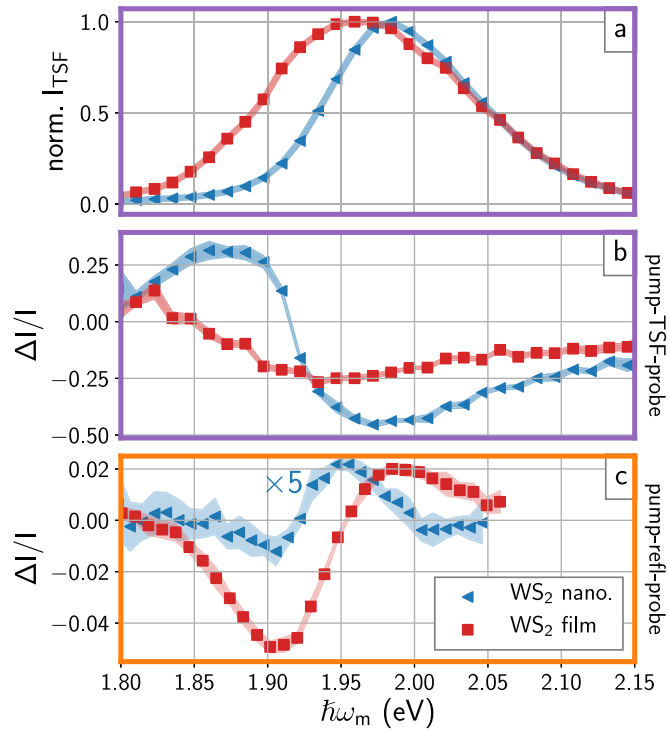

FIG. 11. Comparison of pump-TSF-probe and pump-reflectance-probe for two morphologies of WS_2: a thin film and a single, ∼150 μm wide spiral nanostructure. (a) Normalized TSF spectrum for each sample; these spectra are not normalized for the frequency-dependent intensity of the probe OPA. (b) Pump-TSF-probe spectra for each sample. (c) Pump-refl-probe spectra for each sample. In (b) and (c) the sub-band-edge pump has frequency of $\hbar\omega_{\text{pump}} = 1.054$ eV and a fluence of ∼7000 μJ/cm^2. All spectra were acquired for the same number of laser shots. Each spectrum is composed of 7 spectra averaged together at $T \approx 0.12$ ps. Panels (b) and (c) each show the standard deviation of the averaged spectra for each sample morphology as a filled spread around the average.

cooling to form excitons [89,98]. In TMDCs, hot carriers bleach excitonic transitions more effectively than excitons, so a hot carrier cooling will reduce the bleach observed at the *A* and *B* transitions [89,98,110]. Taken together, we believe defect/grain-boundary assisted quenching of carriers along with hot carrier cooling can explain the dynamics observed in Figs. 9 and 10.

2. *Unified description of pump-induced dynamics in* MoS_2

Our measurements support the following description of carrier dynamics in multilayer MoS_2. The pump creates electrons (holes) in the valence (conduction) band and excitons. These carriers affect the optical transitions that a probe observes. At $T = 0$, the excited carriers screen the electron-hole Coulomb interaction causing BGR and lowering exciton transition energy. The excited carriers also scatter with each other leading to faster dephasing rates and therefore broadening of the exciton transition. The excited carriers can also Pauli-block the band-edge transitions leading to a small decrease in transition amplitude.

After photoexcitation, the carriers are rapidly annihilated, trapped, or scattered to other momentum points (recall that few-layer MoS_2 is an indirect semiconductor). The exact timescale for this relaxation depends on extrinsic properties such as defects: for our polycrystalline thin film the timescale is hundreds of femtoseconds, while for nanostructures the timescale is roughly 10 picoseconds. An electron and hole, once annihilated or trapped, do not scatter or Pauli-block transitions, so the probe sees the original exciton linewidth and transition amplitude. Importantly, a trapped carrier or an indirect exciton can still screen the electron-hole Coulomb interaction [111,112], so a long-lived redshift of the exciton transition is commensurate with residual BGR caused by trapped/indirect carriers. The $T = 0.55$ ps spectrum shown in Fig. 7(b) represents this residual BGR.

3. *Transient-THG vs transient reflectance for* WS_2 *thin film vs single nanostructure*

To further investigate the abilities of pump-TSF-probe, we performed pump-TSF-probe and pump-reflectance-probe experiments on two different morphologies of WS_2: a thin film on a fused silica substrate [photo shown in Fig. 4(a)], and a single, isolated, spiral nanostructure grown on a 300 nm SiO_2 on Si substrate [optical microscope and atomic force microscope characterization shown in Figs. 4(c) and 4(b), respectively]. Our probe beam area is small compared to the area of the thin film, but much larger than the single nanostructure.

In Fig. 11 we use a NIR pump to drive midgap or 2-photon transitions and probe the *A* exciton transition of WS_2. Appendix C describes experiments on our MoS_2 thin film which demonstrate our ability to drive midgap transitions

with a NIR pump. The full spectra and a discussion of these NIR pump measurements will be the subject of another publication. The unpumped THG spectra of the thin film and nanostructure are shown in Fig. 11(a), and the differential spectra ($T = 120$ fs) for each morphology are shown in Fig. 11(b). In both cases, the thin film exhibits a broader and redder A feature than the nanostructure—structural inhomogeneity from the small grain size of the polycrystalline film likely causes the increased linewidth of the thin film. The differing amount of spectral inhomogeneity causes the transient-reflectance and transient-TSF spectra between the two samples to look slightly different.

While the transient-TSF spectra from both the thin film and the single nanostructure are comparable in signal strength, the same is not true for transient-reflectance measurements. Figure 11(c) shows that the nanostructure significantly reduces the transient-reflectance signal (∼5 times less signal). This is largely due to the indiscriminate nature of reflectivity [Eqs. (5)–(9)]: since the bare substrate has a substantial reflectivity and covers a large portion of the illumination area, a correspondingly large portion of the reflected probe does not represent the nanostructure. As a result, the relative change in reflectivity of the nanostructure is diminished. Furthermore, reflected light from bare substrate interferes with reflected light of the nanostructure signals, significantly complicating comparisons between the spectra of the two structures.

In contrast, TSF emission is strongly dependent on resonance enhancement and dipole strength [Eqs. (3) and (10)]. These dependencies strongly suppress both glass substrates (no resonant enhancement) and bulk semiconductor substrates (small dipoles for resonant transitions). As a result, our TSF probe is virtually background free, with contrast similar to that of fluorescence imaging.

V. OUTLOOK AND CONCLUSION

Using the examples of MoS_2 and WS_2, this work shows that pump-TSF-probe spectroscopy can elucidate the dynamics and energetics of photoexcited semiconductor thin films and nanostructures. We demonstrated that this spectroscopy (specifically the degenerate case of pump-TSF-probe, pump-THG-probe) is complementary to the more mature spectroscopy, transient reflectance. While pump-THG-probe and transient reflectance have different dependencies on variables such as transition dipole strength and state density, we showed that the two spectroscopies can be understood in tandem from the same underlying excited-state physics. These differences in dependencies allow pump-TSF-probe to offer a complementary view on excited state physics, which in some cases will be more definitive than a transient-reflectance measurement. We found that transient-TSF is robust to extrinsic nanocrystal properties, such as size and surface coverage, that dramatically affect transient-reflectance spectra. This robustness allowed us to measure the transient-TSF spectrum of nanostructures much smaller than the excitation spot size, while at the same time maintaining a high signal-to-noise ratio. We predict that with pump-TSF-probe spectroscopy, researchers can avoid the reflectance artifacts which have complicated recent ultrafast work (cf. Refs. [113,114]) because the measured TSF and pump-TSF-probe intensities are easily connected to the sample's susceptibility.

Previous studies have shown that TSF can be used to measure coupling between states [21,28]. Isolating cross peaks is a strategy not explored in this work that could further increase the selectivity of pump-TSF-probe spectroscopy in the future. We believe that samples with states/bands of the correct symmetry would yield insightful dynamical coupling information. For instance, since TSF can measure the energy separations of up to four states, it could resolve how bands change their dispersion upon photoexcitation. Crucially, unlike other multidimensional probes which are not fully coherent [2,6,18,19], TSF is not susceptible to population relaxations during the multiple electric field interactions; it is therefore a more direct probe of the underlying quantum states.

Another area that could benefit from the proof-of-concept measurements in this work is multiphoton microscopy. Multiphoton microscopy uses a diverse set of techniques, including THG/TSF [29–31], to predominantly measure biologically relevant samples. These multiphoton microscopies could easily incorporate a pump and a delay stage in order to measure spatially resolved dynamics.

All data and the workup/representation/simulation scripts used to generate the figures in this work are available for download [66].

ACKNOWLEDGMENTS

We acknowledge support from the Department of Energy, Office of Basic Energy Sciences, Division of Materials Sciences and Engineering, under Award No. DE-FG02-09ER46664. D.J.M. acknowledges support from the Link Foundation. We thank Kyle Czech for synthesizing the MoS_2 thin film sample.

D.J.M., D.D.K., and J.C.W. have filed a patent application on some of the work described herein.

APPENDIX A: SINGLE-RESONANCE SIMULATIONS OF PUMP-PROBE RESPONSES

Here we examine the spectra produced by small changes in a system described by one Lorentzian resonance. We assume the system changes are small [Eq. (16)].

1. Pump-THG-probe

The single-resonance third-order susceptibility is given by

$$\chi^{(3)} = \frac{\mu^4}{\omega_{ag} - \omega_{321} - i\Gamma}. \tag{A1}$$

The partial derivatives of Eq. (A1) are

$$\frac{\partial \chi^{(3)}}{\partial \mu} = \frac{4\mu^3}{\omega_{ag} - \omega_{321} - i\Gamma}, \tag{A2}$$

$$\frac{\partial \chi^{(3)}}{\partial \Gamma} = i\frac{\mu^4}{(\omega_{ag} - \omega_{321} - i\Gamma)^2}, \tag{A3}$$

$$\frac{\partial \chi^{(3)}}{\partial \omega_{ag}} = -\frac{\mu^4}{(\omega_{ag} - \omega_{321} - i\Gamma)^2}. \tag{A4}$$

Using Eqs. (12) and (16) we can calculate the change in TSF intensity due to a perturbation:

$$\frac{\Delta I}{I} = \left|1 + \frac{1}{\chi^{(3)}}\frac{\partial \chi^{(3)}}{\partial \lambda} d\lambda\right|^2 - 1 \tag{A5a}$$

$$\approx 2\,\mathrm{Re}\left[\frac{1}{\chi^{(3)}}\frac{\partial \chi^{(3)}}{\partial \lambda}\right] d\lambda, \tag{A5b}$$

where in Eq. (A5b) we used the fact that the perturbation is small, $d\chi^{(3)} \ll \chi^{(3)}$ [Eq. (A5b) is equivalent to Eq. (15)]. Combining Eqs. (A1)–(A5b), we have

$$\frac{\Delta I}{I} \approx 8\frac{d\mu}{\mu}, \quad \lambda = \mu, \tag{A6}$$

$$\frac{\Delta I}{I} \approx -\frac{2\Gamma}{(\omega_{ag} - \omega_{321})^2 + \Gamma^2} d\Gamma \quad (\propto \mathrm{Im}[\chi^{(3)}]), \quad \lambda = \Gamma, \tag{A7}$$

$$\frac{\Delta I}{I} \approx -\frac{2(\omega_{ag} - \omega_{321})}{(\omega_{ag} - \omega_{321})^2 + \Gamma^2} d\omega_{ag} \quad (\propto \mathrm{Re}[\chi^{(3)}]), \quad \lambda = \omega_{ag}. \tag{A8}$$

This is the desired result which was discussed in the main text (Fig. 2).

2. Transient transmittance and transient reflectance

The single-resonance linear susceptibility is given by

$$\chi^{(1)} = \frac{\mu^2}{\omega_{ag} - \omega - i\Gamma}. \tag{A9}$$

The partial derivatives are

$$\frac{\partial \chi^{(1)}}{\partial \mu} = \frac{2\mu}{\omega_{ag} - \omega - i\Gamma} \quad (\propto \chi^{(1)}), \tag{A10}$$

$$\frac{\partial \chi^{(1)}}{\partial \Gamma} = i\frac{\mu^2}{(\omega_{ag} - \omega - i\Gamma)^2} \quad \left(\propto i\frac{d}{d\omega}\chi^{(1)}\right), \tag{A11}$$

$$\frac{\partial \chi^{(1)}}{\partial \omega_{ag}} = -\frac{\mu^2}{(\omega_{ag} - \omega - i\Gamma)^2}. \tag{A12}$$

Using Eq. (12) and the thin film limit Eq. (13), the differential reflectivity for a small change in parameter λ is

$$\frac{\Delta R}{R} = -\frac{R_0}{R}\frac{4\omega\ell}{(1 + n_s^2)c}\mathrm{Im}\left[\frac{\partial \chi^{(1)}}{\partial \lambda} d\lambda\right]. \tag{A13}$$

Since the quantity $\frac{R_0}{R}\frac{4\omega\ell}{(1+n_s^2)c}$ is relatively insensitive to frequency, the differential reflectance line shape can be inferred by examining the imaginary projections of Eqs. (A10)–(A12). The line shape for $\lambda = \mu$ corresponds to the imaginary component of the original Lorentzian line shape. The line shape for $\lambda = \Gamma$ corresponds to the first-derivative line shape of the real (dispersive) part of the resonance. The line shape for $\lambda = \omega_{ag}$ corresponds to the first-derivative line shape of the original Lorentzian.

Finally, note that for transmission that obeys Beer's law ($I = I_0 \exp(-\alpha\ell)$ with $\alpha \equiv \frac{\omega}{cn}\mathrm{Im}[\chi^{(1)}]$, where n is the refractive index of the volume), the expression for a small differential signal differs from Eq. (A13) only by prefactors:

$$\frac{\Delta T}{T} = \frac{\exp(-\alpha_{\mathrm{pumped}}\ell) - \exp(-\alpha_{\mathrm{unpumped}}\ell)}{\exp(-\alpha_{\mathrm{unpumped}}\ell)} \tag{A14}$$

$$\approx -\ell(\alpha_{\mathrm{pumped}} - \alpha_{\mathrm{unpumped}}) \tag{A15}$$

$$= -\frac{\omega\ell}{nc}\mathrm{Im}\left[\frac{\partial \chi^{(1)}}{\partial \lambda} d\lambda\right] \tag{A16}$$

$$= \frac{R}{R_0}\frac{1 + n_s^2}{4n}\frac{\Delta R}{R}, \tag{A17}$$

so $\Delta T/T$ and $\Delta R/R$ are proportional to the extent that R, n, and n_s are frequency invariant. Therefore the transient-reflection line shapes of Fig. 2(a) can be interpreted as the absorption cross section line-shape changes seen in $\Delta T/T$ measurements.

APPENDIX B: LINE-SHAPE MODELING

In this Appendix we describe our simple model for building the spectral line shapes shown in Fig. 7. The general implementation is as follows:

(1) For both spectroscopies construct an unexcited $\chi^{(n)}$ spectrum from a sum of oscillators.

(2) Calculate the unexcited reflectance or TSF spectrum from $\chi^{(1)}$ and $\chi^{(3)}$, respectively.

(3) Create a $\chi^{(n)\prime}$ spectrum to perturb the central frequencies, linewidths, and amplitudes of the oscillators used to construct $\chi^{(n)}$.

(4) Calculate the excited reflectance or TSF spectrum from $\chi^{(1)\prime}$ and $\chi^{(3)\prime}$, respectively.

(5) Use Eq. (12) to calculate $\frac{\Delta I}{I}$ for both spectroscopies.

(6) Iterate through previous steps to fit observed line shapes.

We choose to use complex, Lorentzian oscillators to construct our spectra,

$$\chi^{(n)} = \sum_{j=1} \sqrt{\frac{\Gamma_j}{\pi}}\frac{A_j}{E_{0,j} - \hbar\omega_m - i\Gamma_j}, \tag{B1}$$

in which $j = 1$ and $j = 2$ are the A and B transitions, and the other oscillators are high-lying nonresonant transitions. To create $\chi^{(n)\prime}$ we replace $\Gamma_j \to \Gamma_j + \Delta\Gamma_j$, $E_{0,j} \to E_{0,j} + \Delta E_{0,j}$, and $A_j \to (1 - \text{percent decrease})A_j$. ESA-like additional transitions are incorporated by adding a phased offset to $\chi^{(n)\prime}$; the pump-TSF-probe spectrum in Fig. 7(b) has a slight offset with phase described by $\exp[i\theta]$ with $\theta = 1$ radian. Table II codifies the parameters we found, by hand, to give acceptable fits to the data shown in Fig. 7.

We construct a TSF spectrum by merely calculating the square magnitude of $\chi^{(3)}$ as indicated by Eq. (10). We construct a reflectance spectrum by converting $\chi^{(1)}$ to a complex refractive index, $\bar{n}$, and then using a Fresnel-coefficient-like analysis, specifically as discussed in Anders [115], which takes into account the influence of multiple reflections and the substrate. This treatment is slightly more holistic than merely using Eq. (5) because it takes into account the finite thickness

TABLE II. Parameters used to produce the line shapes shown in Fig. 7. Note that the model in Fig. 7(b) for pump-TSF-probe has a slight offset with phase described by $\exp[i\theta]$ with $\theta = 1$ radian and amplitude of 1% of the maximum feature.

transition	E_0 (eV)	ΔE_0 (eV)	Γ (eV)	$\Delta\Gamma$ (eV)	relative A	% A decrease
			transient-reflectance model $T = 0.05$ ps			
A	1.807	−0.01	0.1	0.002	1	2
B	1.98	−0.009	0.12	0.005	1.1	2
	2.7	−0.008	0.25	0	4	5
	3.2	0	0.25	0	8	0
	6	0	0.25	0	40	0
			transient-reflectance model $T = 0.55$ ps			
A	1.807	−0.005	0.1	0	1	2
B	1.98	−0.005	0.12	0	1.1	2
	2.7	0	0.25	0	4	5
	3.2	0	0.25	0	8	0
	6	0	0.25	0	40	0
			transient-TSF model $T = 0.05$ ps			
A	1.81	−0.012	0.085	0.005	1	2
B	1.95	−0.009	0.1	0.005	0.91	2
			transient-TSF model $T = 0.55$ ps			
A	1.81	−0.003	0.085	0	1	0
B	1.95	−0.002	0.1	0	0.91	0

of the sample [while the derivation of Eq. (5) assumes a delta function sample]. R is calculated using

$$R = \left| \frac{\bar{r}_1 + \bar{r}_2 \exp[-i\phi_1]}{1 + \bar{r}_1\bar{r}_2 \exp[-i\phi_1]} \right|^2, \tag{B2}$$

$$\bar{r}_1 = \frac{\bar{n}_0 - \bar{n}_1}{\bar{n}_0 + \bar{n}_1}, \tag{B3}$$

$$\bar{r}_2 = \frac{\bar{n}_1 - \bar{n}_2}{\bar{n}_1 + \bar{n}_2}, \tag{B4}$$

$$\phi_1 = \frac{4\pi\ell\bar{n}_1}{\lambda}, \tag{B5}$$

in which $\bar{n}_0$ is the refractive index of air, $\bar{n}_1$ is the constructed refractive index of the MoS_2 thin film with thickness ℓ, $\bar{n}_2$ is the refractive index of the fused silica substrate, and λ is the vacuum wavelength of the interrogating electric field.

APPENDIX C: SUB-BAND-GAP PUMP, REFLECTANCE PROBE OF A MoS_2 THIN FILM

TMDCs have weak but finite absorption well below the band gap [116]. To investigate this sub-band-edge response, we tuned our pump to NIR colors, using fluence an order of magnitude higher than the visible pump. The effects of this sub-band-edge pump on the band-edge reflectance spectrum are shown in Fig. 12. We observe similar spectral and temporal line shapes for both the visible and NIR pump, indicating the NIR pump generates photocarriers in a similar manner to a visible pump.

Given the strong two-photon absorption in TMDCs [117–121], it is possible that the signals in Fig. 12 arise from two-photon absorption of sub-band-gap light. To identify the presence of two-photon transitions, we examined the fluence scaling. Figure 13 shows the TR signal scaling for the sub-band-gap pump (orange downward-pointing triangles). We observe linear scaling of the probe metric with respect to the NIR pump fluence. This linear scaling is commensurate with the work of Völzer *et al.* [122], who observe linear response in bulk MoS_2 up to a pump fluence of ~200 $\mu J/cm^2$. These observations rule out two-photon absorption as the dominant contribution to Fig. 12. Instead, it is likely that our NIR pump excites electrons/holes to/from midgap states that have small optical cross sections. Midgap states exist in synthetically grown MoS_2 and are generally attributed to sulfur vacancies and edge defects [91,123–128]. We believe midgap excitations can induce BGR and band filling in a manner similar to direct, allowed transitions, which explains the similarity in line shape between visible and NIR pumps [compare Fig. 8(a)

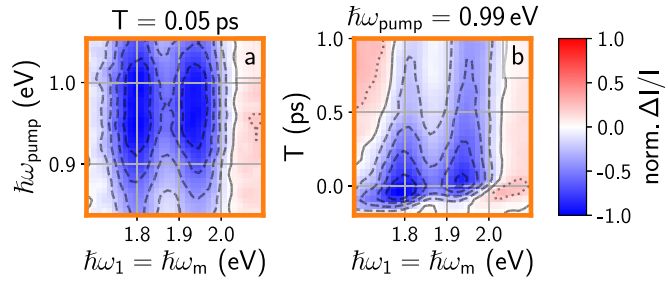

FIG. 12. Transient-reflectance spectroscopy on a MoS_2 thin film with a NIR pump. Panel (a) shows the transient-reflectance spectrum for different combinations of pump and probe frequencies for $T =$ 50 fs. This spectrum is not normalized for the frequency dependence of the pump laser intensity. Panel (b) shows the measured dynamics for different probe colors with $\hbar\omega_{pump} = 0.99$ eV.

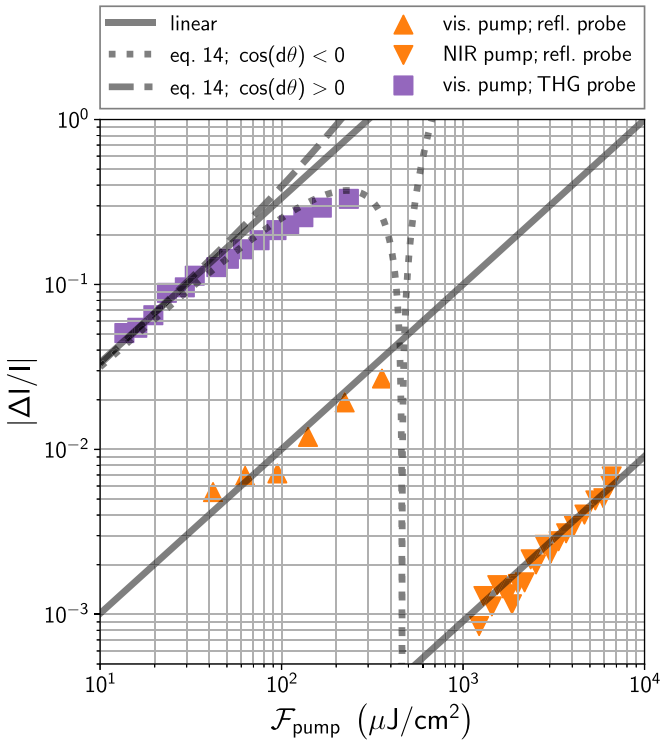

FIG. 13. Comparison of transient-reflectance spectroscopy (orange) to transient-TSF spectroscopy (violet) pump fluence scaling for a MoS_2 thin film. The y axis is the maximum extent of the bleach measured (near $T = 0$). The pump and probe combinations are as follows: (upward-pointing triangles, $\hbar\omega_1 = \hbar\omega_m = \hbar\omega_{\text{pump}} = 1.98$ eV); (downward-pointing triangles, $\hbar\omega_1 = \hbar\omega_m = 1.98$ eV, $\hbar\omega_{\text{pump}} = 0.99$ eV); and (squares, $3\hbar\omega_1 = \hbar\omega_m = 2.05$ eV, $\hbar\omega_{\text{pump}} = 1.98$ eV). Gray solid lines show linear scaling to guide the eye. The gray dotted line is a fit of Eq. (14) to the THG probe data. Also shown is an example of Eq. (14) for the case of constructive interference (dashed line).

with Fig. 12(a) or Fig. 6(a) with Fig. 12(b)]. The insensitivity to pump wavelength reflects the large dispersion of midgap states and their transitions to valence and conduction bands.

APPENDIX D: PUMP-FLUENCE DEPENDENCE OF PUMP-TSF-PROBE

Here we investigate the scaling of the pump-TSF-probe signal with respect to pump fluence. Figure 13 shows the fluence dependence of $|\Delta I_{\text{TSF}}|/I_{\text{TSF}}$ when pumping and probing near the B exciton resonance (purple squares), and compares the response to pump-reflection-probe pumping and probing the same resonance (orange upward-pointing triangles).

The $|\Delta I_{\text{TSF}}|/I_{\text{TSF}}$ shows sublinear behavior at higher fluences (>50 μJ/cm^2). Since the reflection probe exhibits linear response for far higher pump fluences than the onset of THG sublinear scaling, we cannot attribute the sublinear trend to traditional explanations such as band saturation or many-body effects caused by the pump interaction. Rather, we attribute this unique power dependence to the competition between the quadratic-scaling, difference intensity signal, $|d\chi^{(3)}|^2$, and the linear-scaling, heterodyne signal, $|\chi^{(3)}||d\chi^{(3)}|\cos(d\theta)$ [cf. Eq. (14)]. For low pump fluence, $d\chi^{(3)} \ll \chi^{(3)}$ so $|\Delta I_{\text{TSF}}|/I_{\text{TSF}}$ scales linearly. As the pump fluence is increased to the point where $|\Delta I_{\text{TSF}}|/I_{\text{TSF}} \sim 1$, the intensity level differential signal becomes similar to the heterodyne signal, so the quadratic term becomes important. The observed power scaling in this regime depends on the sign of $\cos(d\theta)$, which can be inferred by the sign of ΔI in the linear fluence regime. When $\cos(d\theta) > 0$ (and $\Delta I > 0$ for low fluence), the quadratic term adds to the linear term and superlinear scaling is observed (as simulated in Fig. 13, hashed line). When $\cos(d\theta) < 0$ (and $\Delta I < 0$ for low fluence, as is the case in Fig. 13), the quadratic term and linear-scaling term destructively interfere and sublinear scaling is observed (as simulated in Fig. 13, dotted line). Note that the Eq. (14) fit of our pump-TSF-probe fluence data recovers the phase and amplitude of $\chi^{(5)} = d\chi^{(3)}/\mathcal{F}_{\text{pump}}$: we find that $|\chi^{(5)}|/|\chi^{(3)}| = 0.003$ cm$^2/\mu$J and $\cos(d\theta) = -0.6$.

Theoretically, a power scaling competition similar to Eq. (14) can occur in linear probe experiments if $d\chi^{(1)}$ becomes large enough, but this regime is uncommon because in linear experiments the unpumped probe (reflection or transmission) is usually more intense, so higher-order pump processes often contribute before this onset. For example in Fig. 13, a pump fluence of $\sim$100 μJ/cm^2 produces only a $\sim$1% change in reflectivity, while under the same conditions the TSF intensity changes by $\sim$20%.

To reiterate, the pump-TSF-probe fluence scaling is both nonlinear and well understood; the trend is *not* due to higher-order nonlinear effects (e.g., $\chi^{(7)}$). The pump fluence trends observed here are well described by a fluence-independent absorption cross section for the pump. Note that the line shape simulations in Fig. 2 assume linear scaling of pump fluence. Our main results were acquired at a pump fluence of $\sim$100 μJ/cm^2 which is in the regime of nonlinear scaling of $|\Delta I_{\text{TSF}}|/I_{\text{TSF}}$ with pump fluence. Importantly, the line-shape fitting of our data (Fig. 7) accounts for the possible nonlinear scaling of $|\Delta I_{\text{TSF}}|/I_{\text{TSF}}$ with pump fluence because Eq. (12) is explicitly used in our model. If we had used Eq. (15) in our analysis this nonlinear pump scaling would not have been taken into account.

[1] R. Ulbricht, E. Hendry, J. Shan, T. F. Heinz, and M. Bonn, Rev. Mod. Phys. **83**, 543 (2011).
[2] W. Xiong, J. E. Laaser, P. Paoprasert, R. A. Franking, R. J. Hamers, P. Gopalan, and M. T. Zanni, J. Am. Chem. Soc. **131**, 18040 (2009).
[3] D. R. Dietze and R. A. Mathies, ChemPhysChem **17**, 1224 (2016).
[4] A. E. Bragg, W. Yu, J. Zhou, and T. Magnanelli, J. Phys. Chem. Lett. **7**, 3990 (2016).
[5] F. Ceballos, M.-G. Ju, S. D. Lane, X. C. Zeng, and H. Zhao, Nano Lett. **17**, 1623 (2017).
[6] A. Mandal, J. D. Schultz, Y.-L. Wu, A. F. Coleman, R. M. Young, and M. R. Wasielewski, J. Phys. Chem. Lett. **10**, 3509 (2019).

[7] E. J. Sie, C. M. Nyby, C. D. Pemmaraju, S. J. Park, X. Shen, J. Yang, M. C. Hoffmann, B. K. Ofori-Okai, R. Li, A. H. Reid, S. Weathersby, E. Mannebach, N. Finney, D. Rhodes, D. Chenet, A. Antony, L. Balicas, J. Hone, T. P. Devereaux, T. F. Heinz, X. Wang, and A. M. Lindenberg, Nature (London) **565**, 61 (2019).

[8] F. Liu, M. E. Ziffer, K. R. Hansen, J. Wang, and X. Zhu, Phys. Rev. Lett. **122**, 246803 (2019).

[9] F. Langer, C. P. Schmid, S. Schlauderer, M. Gmitra, J. Fabian, P. Nagler, C. Schüller, T. Korn, P. G. Hawkins, J. T. Steiner, U. Huttner, S. W. Koch, M. Kira, and R. Huber, Nature (London) **557**, 76 (2018).

[10] Z. Wang, H. Park, Y. H. Lai, J. Xu, C. I. Blaga, F. Yang, P. Agostini, and L. F. DiMauro, Nat. Commun. **8**, 1686 (2017).

[11] J. C. Wright, Annu. Rev. Phys. Chem. **62**, 209 (2011).

[12] J. C. Wright, Annu. Rev. Anal. Chem. **10**, 45 (2017).

[13] P. C. Chen, Appl. Spectrosc. **70**, 1937 (2016).

[14] C. L. Smallwood and S. T. Cundiff, Laser Photonics Rev. **12**, 1800171 (2018).

[15] S. T. Cundiff and S. Mukamel, Phys. Today **66**(7), 44 (2013).

[16] M. Cho, Chem. Rev. **108**, 1331 (2008).

[17] M. Cho (Ed.), *Coherent Multidimensional Spectroscopy* (Springer Singapore, 2019).

[18] J. Bredenbeck, J. Helbing, R. Behrendt, C. Renner, L. Moroder, J. Wachtveitl, and P. Hamm, J. Phys. Chem. B **107**, 8654 (2003).

[19] B. Abraham, L. G. C. Rego, and L. Gundlach, J. Phys. Chem. C **123**, 23760 (2019).

[20] N. A. Neff-Mallon and J. C. Wright, Anal. Chem. **89**, 13182 (2017).

[21] J. D. Handali, K. F. Sunden, B. J. Thompson, N. A. Neff-Mallon, E. M. Kaufman, T. C. Brunold, and J. C. Wright, J. Phys. Chem. A **122**, 9031 (2018).

[22] E. S. Boyle, A. V. Pakoulev, and J. C. Wright, J. Phys. Chem. A **117**, 5578 (2013).

[23] E. S. Boyle, N. A. Neff-Mallon, and J. C. Wright, J. Phys. Chem. A **117**, 12401 (2013).

[24] E. S. Boyle, N. A. Neff-Mallon, J. D. Handali, and J. C. Wright, J. Phys. Chem. A **118**, 3112 (2014).

[25] M. Grechko, T. Hasegawa, F. D'Angelo, H. Ito, D. Turchinovich, Y. Nagata, and M. Bonn, Nat. Commun. **9**, 885 (2018).

[26] M. Bonn, C. Hess, J. H. Miners, T. F. Heinz, H. J. Bakker, and M. Cho, Phys. Rev. Lett. **86**, 1566 (2001).

[27] D. J. Morrow, D. D. Kohler, K. J. Czech, and J. C. Wright, J. Chem. Phys. **149**, 091101 (2018).

[28] M. Grechko, S. A. Bretschneider, L. Vietze, H. Kim, and M. Bonn, Angew. Chem. **57**, 13657 (2018).

[29] A. M. Hanninen, R. C. Prince, and E. Potma, IEEE J. Sel. Top. Quantum Electron. **25**, 1 (2018).

[30] A. M. Hanninen, R. C. Prince, R. Ramos, M. V. Plikus, and E. O. Potma, Biomed. Opt. Express **9**, 4807 (2018).

[31] H. Segawa, M. Okuno, H. Kano, P. Leproux, V. Couderc, and H. Hamaguchi, Opt. Express **20**, 9551 (2012).

[32] K. F. Mak, C. Lee, J. Hone, J. Shan, and T. F. Heinz, Phys. Rev. Lett. **105**, 136805 (2010).

[33] G. Wang, A. Chernikov, M. M. Glazov, T. F. Heinz, X. Marie, T. Amand, and B. Urbaszek, Rev. Mod. Phys. **90**, 021001 (2018).

[34] A. Molina-Sánchez, D. Sangalli, K. Hummer, A. Marini, and L. Wirtz, Phys. Rev. B **88**, 045412 (2013).

[35] D. Y. Qiu, F. H. da Jornada, and S. G. Louie, Phys. Rev. Lett. **111**, 216805 (2013).

[36] K. He, N. Kumar, L. Zhao, Z. Wang, K. F. Mak, H. Zhao, and J. Shan, Phys. Rev. Lett. **113**, 026803 (2014).

[37] N. Saigal, V. Sugunakar, and S. Ghosh, Appl. Phys. Lett. **108**, 132105 (2016).

[38] J. Kopaczek, M. P. Polak, P. Scharoch, K. Wu, B. Chen, S. Tongay, and R. Kudrawiec, J. Appl. Phys. **119**, 235705 (2016).

[39] A. Autere, H. Jussila, Y. Dai, Y. Wang, H. Lipsanen, and Z. Sun, Adv. Mater. **30**, 1705963 (2018).

[40] Y. M. Chang, L. Xu, and H. W. K. Tom, Phys. Rev. Lett. **78**, 4649 (1997).

[41] C. Guo, G. Rodriguez, and A. J. Taylor, Phys. Rev. Lett. **86**, 1638 (2001).

[42] A. McClelland, V. Fomenko, and E. Borguet, J. Phys. Chem. B **108**, 3789 (2004).

[43] D. Hsieh, F. Mahmood, J. W. McIver, D. R. Gardner, Y. S. Lee, and N. Gedik, Phys. Rev. Lett. **107**, 077401 (2011).

[44] W. A. Tisdale, K. J. Williams, B. A. Timp, D. J. Norris, E. S. Aydil, and X.-Y. Zhu, Science **328**, 1543 (2010).

[45] H. Park, M. Gutierrez, X. Wu, W. Kim, and X.-Y. Zhu, J. Phys. Chem. C **117**, 10974 (2013).

[46] C. A. Nelson, J. Luo, A. K.-Y. Jen, R. B. Laghumavarapu, D. L. Huffaker, and X.-Y. Zhu, J. Phys. Chem. C **118**, 27981 (2014).

[47] E. M. Mannebach, K.-A. N. Duerloo, L. A. Pellouchoud, M.-J. Sher, S. Nah, Y.-H. Kuo, Y. Yu, A. F. Marshall, L. Cao, E. J. Reed, and A. M. Lindenberg, ACS Nano **8**, 10734 (2014).

[48] K. J. Czech, B. J. Thompson, S. Kain, Q. Ding, M. J. Shearer, R. J. Hamers, S. Jin, and J. C. Wright, ACS Nano **9**, 12146 (2015).

[49] J. P. Lomont, K. L. Rich, M. Maj, J.-J. Ho, J. S. Ostrander, and M. T. Zanni, J. Phys. Chem. B **122**, 144 (2017).

[50] A. M. Alperstein, J. S. Ostrander, T. O. Zhang, and M. T. Zanni, Proc. Natl. Acad. Sci. USA **116**, 6602 (2019).

[51] D. J. Morrow, D. D. Kohler, and J. C. Wright, Phys. Rev. A **96**, 063835 (2017).

[52] N. Bloembergen and P. S. Pershan, Phys. Rev. **128**, 606 (1962).

[53] A. Taghizadeh and T. G. Pedersen, Phys. Rev. B **99**, 235433 (2019).

[54] A. Taghizadeh and T. G. Pedersen, Phys. Rev. B **97**, 205432 (2018).

[55] A. Taghizadeh, F. Hipolito, and T. G. Pedersen, Phys. Rev. B **96**, 195413 (2017).

[56] T. G. Pedersen, Phys. Rev. B **92**, 235432 (2015).

[57] D. B. S. Soh, C. Rogers, D. J. Gray, E. Chatterjee, and H. Mabuchi, Phys. Rev. B **97**, 165111 (2018).

[58] R. W. Boyd, *Nonlinear Optics*, 3rd ed. (Academic Press, 2008).

[59] N. Bloembergen and Y. R. Shen, Phys. Rev. **133**, A37 (1964).

[60] L. A. Falkovsky, J. Phys.: Conf. Ser. **129**, 012004 (2008).

[61] E. J. Sie, A. J. Frenzel, Y.-H. Lee, J. Kong, and N. Gedik, Phys. Rev. B **92**, 125417 (2015).

[62] A. Splendiani, L. Sun, Y. Zhang, T. Li, J. Kim, C.-Y. Chim, G. Galli, and F. Wang, Nano Lett. **10**, 1271 (2010).

[63] A crucial filter for our TSF probe experiments is a 1000 nm long-pass filter (ThorLabs FGL1000M) which ensures no visible light from secondary OPA processes reach the sample.

Notably, double side polished silicon was not a suitable filter because it created non-negligible THG as well as lossy transmission.

[64] K. Furuta, M. Fuyuki, and A. Wada, Appl. Spectrosc. **66**, 1475 (2012).

[65] J. D. Handali, K. F. Sunden, E. M. Kaufman, and J. C. Wright, Chem. Phys. **512**, 13 (2018).

[66] D. J. Morrow, Open Science Framework, 2019, http://dx.doi.org/10.17605/OSF.IO/UMSXC.

[67] B. J. Thompson, K. F. Sunden, D. J. Morrow, and N. A. Neff-Mallon, PyCMDS, 2018, http://dx.doi.org/10.5281/zenodo.1198911.

[68] B. Thompson, K. Sunden, D. Morrow, D. Kohler, and J. Wright, J. Open Source Softw. **4**, 1141 (2019).

[69] E. Jones, T. Oliphant, and P. Peterson, SciPy: Open source scientific tools for python, http://www.scipy.org/.

[70] S. van der Walt, S. C. Colbert, and G. Varoquaux, Comput. Sci. Eng. **13**, 22 (2011).

[71] J. D. Hunter, Comput. Sci. Eng. **9**, 90 (2007).

[72] Y. Zhao and S. Jin, ACS Materials Lett. **2**, 42 (2020).

[73] C. Lee, H. Yan, L. E. Brus, T. F. Heinz, J. Hone, and S. Ryu, ACS Nano **4**, 2695 (2010).

[74] H. Li, Q. Zhang, C. C. R. Yap, B. K. Tay, T. H. T. Edwin, A. Olivier, and D. Baillargeat, Adv. Funct. Mater. **22**, 1385 (2012).

[75] A. Berkdemir, H. R. Gutiérrez, A. R. Botello-Méndez, N. Perea-López, A. L. Elías, C.-I. Chia, B. Wang, V. H. Crespi, F. López-Urías, J.-C. Charlier, H. Terrones, and M. Terrones, Sci. Rep. **3**, 1755 (2013).

[76] M. J. Shearer, L. Samad, Y. Zhang, Y. Zhao, A. Puretzky, K. W. Eliceiri, J. C. Wright, R. J. Hamers, and S. Jin, J. Am. Chem. Soc. **139**, 3496 (2017).

[77] X. Fan, Y. Zhao, W. Zheng, H. Li, X. Wu, X. Hu, X. Zhang, X. Zhu, Q. Zhang, X. Wang, B. Yang, J. Chen, S. Jin, and A. Pan, Nano Lett. **18**, 3885 (2018).

[78] X. Fan, Y. Jiang, X. Zhuang, H. Liu, T. Xu, W. Zheng, P. Fan, H. Li, X. Wu, X. Zhu, Q. Zhang, H. Zhou, W. Hu, X. Wang, L. Sun, X. Duan, and A. Pan, ACS Nano **11**, 4892 (2017).

[79] L. Zhang, K. Liu, A. B. Wong, J. Kim, X. Hong, C. Liu, T. Cao, S. G. Louie, F. Wang, and P. Yang, Nano Lett. **14**, 6418 (2014).

[80] H. Zhang, Y. Wan, Y. Ma, W. Wang, Y. Wang, and L. Dai, Appl. Phys. Lett. **107**, 101904 (2015).

[81] M. M. Benameur, B. Radisavljevic, J. S. Héron, S. Sahoo, H. Berger, and A. Kis, Nanotechnology **22**, 125706 (2011).

[82] P. Blake, E. W. Hill, A. H. Castro Neto, K. S. Novoselov, D. Jiang, R. Yang, T. J. Booth, and A. K. Geim, Appl. Phys. Lett. **91**, 063124 (2007).

[83] R. Wang, H.-C. Chien, J. Kumar, N. Kumar, H.-Y. Chiu, and H. Zhao, ACS Appl. Mater. Interfaces **6**, 314 (2013).

[84] E. A. A. Pogna, M. Marsili, D. D. Fazio, S. D. Conte, C. Manzoni, D. Sangalli, D. Yoon, A. Lombardo, A. C. Ferrari, A. Marini, G. Cerullo, and D. Prezzi, ACS Nano **10**, 1182 (2016).

[85] A. Chernikov, C. Ruppert, H. M. Hill, A. F. Rigosi, and T. F. Heinz, Nat. Photonics **9**, 466 (2015).

[86] A. Steinhoff, M. Rösner, F. Jahnke, T. O. Wehling, and C. Gies, Nano Lett. **14**, 3743 (2014).

[87] L. Meckbach, T. Stroucken, and S. W. Koch, Appl. Phys. Lett. **112**, 061104 (2018).

[88] S. Sim, J. Park, J.-G. Song, C. In, Y.-S. Lee, H. Kim, and H. Choi, Phys. Rev. B **88**, 075434 (2013).

[89] P. D. Cunningham, A. T. Hanbicki, K. M. McCreary, and B. T. Jonker, ACS Nano **11**, 12601 (2017).

[90] Because these line shapes are not merely caused by amplitude changes (J or μ), fitting different probe colors results in different decay rates, with τ up to 0.4 ps.

[91] P. D. Cunningham, K. M. McCreary, A. T. Hanbicki, M. Currie, B. T. Jonker, and L. M. Hayden, J. Phys. Chem. C **120**, 5819 (2016).

[92] H. Shi, R. Yan, S. Bertolazzi, J. Brivio, B. Gao, A. Kis, D. Jena, H. G. Xing, and L. Huang, ACS Nano **7**, 1072 (2013).

[93] P. Schiettecatte, P. Geiregat, and Z. Hens, J. Phys. Chem. C **123**, 10571 (2019).

[94] D. Tsokkou, X. Yu, K. Sivula, and N. Banerji, J. Phys. Chem. C **120**, 23286 (2016).

[95] Z. Nie, R. Long, L. Sun, C.-C. Huang, J. Zhang, Q. Xiong, D. W. Hewak, Z. Shen, O. V. Prezhdo, and Z.-H. Loh, ACS Nano **8**, 10931 (2014).

[96] N. Kumar, J. He, D. He, Y. Wang, and H. Zhao, J. Appl. Phys. **113**, 133702 (2013).

[97] Z. Nie, R. Long, J. S. Teguh, C.-C. Huang, D. W. Hewak, E. K. L. Yeow, Z. Shen, O. V. Prezhdo, and Z.-H. Loh, J. Phys. Chem. C **119**, 20698 (2015).

[98] F. Ceballos, Q. Cui, M. Z. Bellus, and H. Zhao, Nanoscale **8**, 11681 (2016).

[99] A. Singh, G. Moody, S. Wu, Y. Wu, N. J. Ghimire, J. Yan, D. G. Mandrus, X. Xu, and X. Li, Phys. Rev. Lett. **112**, 216804 (2014).

[100] G. Moody, C. K. Dass, K. Hao, C.-H. Chen, L.-J. Li, A. Singh, K. Tran, G. Clark, X. Xu, G. Berghäuser, E. Malic, A. Knorr, and X. Li, Nat. Commun. **6**, 8315 (2015).

[101] A. Singh, G. Moody, K. Tran, M. E. Scott, V. Overbeck, G. Berghäuser, J. Schaibley, E. J. Seifert, D. Pleskot, N. M. Gabor, J. Yan, D. G. Mandrus, M. Richter, E. Malic, X. Xu, and X. Li, Phys. Rev. B **93**, 041401(R) (2016).

[102] K. Hao, G. Moody, F. Wu, C. K. Dass, L. Xu, C.-H. Chen, L. Sun, M.-Y. Li, L.-J. Li, A. H. MacDonald, and X. Li, Nat. Phys. **12**, 677 (2016).

[103] K. Hao, L. Xu, P. Nagler, A. Singh, K. Tran, C. K. Dass, C. Schüller, T. Korn, X. Li, and G. Moody, Nano Lett. **16**, 5109 (2016).

[104] K. Hao, J. F. Specht, P. Nagler, L. Xu, K. Tran, A. Singh, C. K. Dass, C. Schüller, T. Korn, M. Richter, A. Knorr, X. Li, and G. Moody, Nat. Commun. **8**, 15552 (2017).

[105] L. Guo, M. Wu, T. Cao, D. M. Monahan, Y.-H. Lee, S. G. Louie, and G. R. Fleming, Nat. Phys. **15**, 228 (2018).

[106] The decrease in $\Delta I/I$ at high pump frequencies in the TR experiment, Fig. 8(a), is likely caused by a decrease in the I_{pump} at those frequencies. The two spectra in Fig. 8 were collected at different times and do not share the same pump intensity spectrum.

[107] F. Mahmood, Z. Alpichshev, Y.-H. Lee, J. Kong, and N. Gedik, Nano Lett. **18**, 223 (2017).

[108] L. Yang, N. A. Sinitsyn, W. Chen, J. Yuan, J. Zhang, J. Lou, and S. A. Crooker, Nat. Phys. **11**, 830 (2015).

[109] G. Moody, J. Schaibley, and X. Xu, J. Opt. Soc. Am. B **33**, C39 (2016).

[110] S. Schmitt-Rink, D. S. Chemla, and D. A. B. Miller, Phys. Rev. B **32**, 6601 (1985).

[111] P. W. Juodawlkis and S. E. Ralph, Appl. Phys. Lett. **76**, 1722 (2000).
[112] G. Mak and H. M. van Driel, Phys. Rev. B **49**, 16817 (1994).
[113] J. Liu, J. Leng, S. Wang, J. Zhang, and S. Jin, J. Phys. Chem. Lett. **10**, 97 (2019).
[114] T. Ghosh, S. Aharon, A. Shpatz, L. Etgar, and S. Ruhman, ACS Nano **12**, 5719 (2018).
[115] H. Anders, *Thin Films in Optics* (The Focal Press, 1967).
[116] S. Bikorimana, P. Lama, A. Walser, R. Dorsinville, S. Anghel, A. Mitioglu, A. Micu, and L. Kulyuk, Opt. Express **24**, 20685 (2016).
[117] S. Zhang, N. Dong, N. McEvoy, M. O'Brien, S. Winters, N. C. Berner, C. Yim, Y. Li, X. Zhang, Z. Chen, L. Zhang, G. S. Duesberg, and J. Wang, ACS Nano **9**, 7142 (2015).
[118] Z. Ye, T. Cao, K. O'Brien, H. Zhu, X. Yin, Y. Wang, S. G. Louie, and X. Zhang, Nature (London) **513**, 214 (2014).
[119] T. C. Berkelbach, M. S. Hybertsen, and D. R. Reichman, Phys. Rev. B **92**, 085413 (2015).
[120] N. Dong, Y. Li, S. Zhang, N. McEvoy, R. Gatensby, G. S. Duesberg, and J. Wang, ACS Photonics **5**, 1558 (2018).
[121] Q. Cui, Y. Li, J. Chang, H. Zhao, and C. Xu, Laser Photonics Rev. **13**, 1800225 (2018).
[122] T. Völzer, M. Lütgens, F. Fennel, and S. Lochbrunner, J. Phys. B **50**, 194003 (2017).
[123] A. M. van der Zande, P. Y. Huang, D. A. Chenet, T. C. Berkelbach, Y. You, G.-H. Lee, T. F. Heinz, D. R. Reichman, D. A. Muller, and J. C. Hone, Nat. Mater. **12**, 554 (2013).
[124] W. Zhou, X. Zou, S. Najmaei, Z. Liu, Y. Shi, J. Kong, J. Lou, P. M. Ajayan, B. I. Yakobson, and J.-C. Idrobo, Nano Lett. **13**, 2615 (2013).
[125] Z. G. Yu, Y.-W. Zhang, and B. I. Yakobson, Nano Lett. **15**, 6855 (2015).
[126] J. Hong, Z. Hu, M. Probert, K. Li, D. Lv, X. Yang, L. Gu, N. Mao, Q. Feng, L. Xie, J. Zhang, D. Wu, Z. Zhang, C. Jin, W. Ji, X. Zhang, J. Yuan, and Z. Zhang, Nat. Commun. **6**, 6293 (2015).
[127] H. Qiu, T. Xu, Z. Wang, W. Ren, H. Nan, Z. Ni, Q. Chen, S. Yuan, F. Miao, F. Song, G. Long, Y. Shi, L. Sun, J. Wang, and X. Wang, Nat. Commun. **4**, 2642 (2013).
[128] C.-P. Lu, G. Li, J. Mao, L.-M. Wang, and E. Y. Andrei, Nano Lett. **14**, 4628 (2014).